PHYSICS

^{13}C hyperpolarization with nitrogen-vacancy centers in micro- and nanodiamonds for sensitive magnetic resonance applications

Rémi Blinder[1]*, Yuliya Mindarava[1], Martin Korzeczek[2], Alastair Marshall[3]†, Felix Glöckler[4]‡, Steffen Nothelfer[4]§, Alwin Kienle[4], Christian Laube[5], Wolfgang Knolle[5], Christian Jentgens[6], Martin B. Plenio[2,7], Fedor Jelezko[1,7]

Nuclear hyperpolarization is a known method to enhance the signal in nuclear magnetic resonance (NMR) by orders of magnitude. The present work addresses the ^{13}C hyperpolarization in diamond micro- and nanoparticles, using the optically pumped nitrogen-vacancy center (NV) to polarize ^{13}C spins at room temperature. Consequences of the small particle size are mitigated by using a combination of surface treatment improving the ^{13}C relaxation (T_1) time, as well as that of NV, and applying a technique for NV illumination based on a microphotonic structure. Adjustments to the dynamical nuclear polarization sequence (PulsePol) are performed, as well as slow sample rotation, to improve the NV-^{13}C polarization transfer rate. The hyperpolarized ^{13}C NMR signal is observed in particles of 2-micrometer and 100-nanometer median sizes, with enhancements over the thermal signal (at 0.29-tesla magnetic field) of 1500 and 940, respectively. The present demonstration of room-temperature hyperpolarization anticipates the development of agents based on nanoparticles for sensitive magnetic resonance applications.

INTRODUCTION

As a technique improving the sensitivity of nuclear magnetic resonance (NMR) and magnetic resonance imaging (MRI), hyperpolarization is widely explored for enhancing the acquisition of the nuclear precession signal (*1*). Besides its applications in medical imaging (*2*, *3*), it holds the promise of benefiting multiple research fields including metabolomics (*4*), drug screening and monitoring (*5*, *6*), the study of proteins (*7*), nano/mesoporous systems (*8*), or battery materials (*9*). Signal enhancements by above four orders of magnitude were demonstrated in the work of Ardenkjær-Larsen *et al.* (*10*), using the method, nowadays known as dissolution dynamical nuclear polarization (DNP), which enabled in vivo imaging of metabolic processes (*11*). Despite these accomplishments, alternative concepts are being investigated, with the prospect of reducing hardware cost and complexity (that are both elevated in dissolution DNP because of the use of cryogens) or bringing magnetic resonance signal boosts to new systems. To circumvent the need for cryogenic temperatures yet achieve high nuclear signal enhancements, a proposed approach is the use of DNP protocols with electrons that are initialized out of equilibrium, in a spin state with above-thermal polarization. Early on, in 1990, this was demonstrated by Henstra *et al.* (*12*), who used the photoexcited state of pentacene molecules in naphthalene to produce high nuclear spin polarization at room temperature. In recent developments, the same method was successfully applied to polarize other matrices (*13*, *14*), and its combination with nuclear Overhauser effect enhancement in the liquid state was demonstrated, allowing for polarization of external substances (*15*, *16*).

An interesting prospect in terms of novel applications of DNP is the generation of hyperpolarization within nanoparticles (<200 nm). This stems from the following reasons: (i) Such nanoparticles can diffuse efficiently by circulation in the blood flow (*17*), making them candidate for the application as MRI tracers; and (ii) owing to the high surface-to-volume ratio, they could play the role of renewable source of polarization for external substances. The possibility of performing MRI acquisitions enhanced by hyperpolarization was demonstrated with ^{13}C in diamond (*18*, *19*) or ^{29}Si in silicon (*20*) nanoparticles, both polarized from thermally polarized endogenous spin defects in a cryogenic environment, at liquid Helium temperatures. Although this scheme performs well under the cryogenic setting, it shows limited efficiency under ambient conditions.

Nanodiamonds attract interest because of several factors, that is, the long ^{13}C spin polarization lifetime (T_1) in diamond (*21*), the good biocompatibility (*22*), and the possibility of producing single-crystalline nanoparticles with lattice properties similar to bulk (*23*). Diamond can also host a wide variety of paramagnetic defects (*24*) that can be used for DNP. One example is the substitutional nitrogen or P1 center ($S = {}^1/_2$) (*25*–*27*), which is incorporated during growth. Specifically in nanodiamonds, near-surface spin defects (*28*, *29*) have also been used (*18*, *19*, *30*, *31*). Last, hyperpolarization was demonstrated using the nitrogen-vacancy center (NV), either in bulk crystal (*32*–*35*) or diamond powder (>1-μm particles) (*36*–*38*). DNP techniques relying on the NV spin, $S = 1$, draw on the essential capability that it can be initialized to a high degree (up to 92%) into the $m_s = 0$ state (*39*), upon excitation with short pulses of green light, at arbitrary magnetic field and ambient conditions. By combining optical pumping with dynamical nuclear polarization, it becomes possible to transfer the spin polarization generated on

[1]Institute for Quantum Optics, Albert-Einstein Allee 11, Ulm University, 89081 Ulm, Germany. [2]Institute of Theoretical Physics, Albert-Einstein Allee 11, Ulm University, 89081 Ulm, Germany. [3]NVision Imaging Technologies GmbH, 89081 Ulm, Germany. [4]Institute for Laser Technologies in Medicine and Metrology at the University of Ulm (ILM), Helmholtzstr. 12, 89081 Ulm, Germany. [5]Leibniz Institute of Surface Engineering, 04318 Leipzig, Germany. [6]Pureon AG, Kreuzlingerstrasse 1, 8574 Lengwil, Switzerland. [7]Centre for Integrated Quantum Science and Technology (IQST), 89081 Ulm, Germany.
*Corresponding author. Email: remi.blinder@uni-ulm.de
†Present address: Qruise GmbH, Am Hölzersbach 7, 66113 Saarbrücken, Germany.
‡Present address: Sensific GmbH, 89081 Ulm, Germany.
§Present address: Hensoldt, Wörthstraße 85, 89077 Ulm, Germany.

the NV to surrounding nuclei. Harnessing NV as a polarization source holds the potential to push the boundaries of conventional DNP methods. This approach could potentially achieve high levels of nuclear polarization, without the requirement of cryogenic temperatures.

However, material and DNP protocols must be optimized to fulfill requirements of using color centers in nanoparticles, such as NV in nanodiamonds. Previous attempts to hyperpolarize ^{13}C spins from NV in diamond nanocrystals (<200 nm) resulted in only a very low degree of nuclear polarization (*37*, *38*). In this work, we address the primary challenges affecting the efficiency of nuclear hyperpolarization in nanodiamonds. First, we mitigate the impact of surface magnetic noise on ^{13}C relaxation time by appropriate surface treatment. Second, we enhance NV initialization by improving sample illumination. Furthermore, we increase the number of NV that is involved simultaneously in polarization transfer to nuclear spins by adjusting parameters in a DNP sequence (PulsePol) (*40*) to enhance its robustness to the orientation-induced broadening of the NV spectrum in powder samples. Last, we implement slow sample rotation (≲25°/s) to bring different subsets of NV into the excitation region of the adapted DNP sequence and cycle through all of them. Thanks to these improvements, we achieve efficient polarization transfer from NV to ^{13}C spins within diamond particles of 2-μm and 100-nm typical sizes, resulting in NMR signal enhancements over the thermal signal of 1500 and 940, respectively, at the polarization field of about 0.29 T.

RESULTS

In this work, we use milled high-pressure high-temperature (HPHT) diamond powders from Pureon AG (Lengwil, Switzerland) with median sizes of about 2 μm and 100 nm (see section S1 for size distribution parameters). Substitutional nitrogens (P1 centers) are converted into NV by high-energy electron irradiation and annealing, as described in a previous work (*41*). In this process, oxidation at high temperature (620°C) in air is performed to remove graphitic residues (*42*). Besides the resulting NV concentrations, given in Table 1, we also consider the ^{13}C spin-lattice relaxation time ($^{13C}T_1$), which is a crucial parameter for hyperpolarization experiments. The $^{13C}T_1$ determines not only the attainable level of nuclear hyperpolarization but also the duration allowed between hyperpolarization and signal detection in the investigated sample. While microdiamonds are expected to exhibit a $^{13C}T_1$ as in bulk crystals of similar defect composition, the spin-lattice relaxation in nanodiamonds (<200 nm) typically shows contributions related to surface spins [dangling bonds, etc.; (*43*)]. In such small particles, to prolong the $^{13C}T_1$, it is thus important to work toward suppression of the surface magnetic noise. Besides the air oxidation (AO), our 100-nm particles were as well treated with a three-acid mixture, as detailed in Materials and Methods. Although acid cleaning and AO are commonly used for nanodiamond surface treatment, to our knowledge, no detailed study has explored the combined effect of both techniques on milled HPHT nanodiamonds, particularly their impact on $^{13C}T_1$ times at room temperature. Here, we investigated the NMR $^{13C}T_1$ at different stages of treatment of the commercial nanodiamonds. The data in Fig. 1A were acquired at $B = 7.05$ T magnetic field, providing evidence that removal of relaxation-inducing sources is better achieved through the combination of AO and triacid cleaning (TAC), rather than by performing each treatment separately. The combination (AO + TAC) leads to $^{13C}T_1 = 152 \pm 12$ s at 7.05 T, which constitutes an improvement by over a factor of 7 with respect to the base commercial material ($^{13C}T_1 = 21 \pm 1$ s). That improvement is dominantly accounted for by the TAC (leading alone to an about fourfold increase). We explain these results as follows: AO achieves a first part of the required surface cleaning by efficiently removing the surface graphite and the related dangling bonds (*42*, *44*). The TAC achieves an important second part by removing paramagnetic metallic residues. The iron element could be detected by x-ray photoelectron spectroscopy (XPS) on smaller nanodiamonds from the same manufacturer and thus constitutes the most likely origin of the magnetic noise that is removed by acid cleaning (see section S2.4).

To investigate further the impact of the acid treatment step, we measure the longitudinal relaxation time of NV ($^{NV}T_1$) by pulsed electron paramagnetic resonance (EPR) on the air-oxidized sample, before and after acid cleaning. From the results shown in Fig. 1B, it can be seen that the combined treatment of AO and acid cleaning prolongs $^{NV}T_1$ by more than a factor of 2, compared to AO alone (Table 1). We correlate this observation with the disappearance of a broad (~3000 G) signal in X-band EPR that we attribute to the removal of the iron impurities (section S2.1). Here, observing the short $^{NV}T_1$ before the treatment with acid as in Fig. 1B is a telltale sign of magnetic noise extending in the high-frequency (approximately gigahertz) range, thereby affecting the relaxation of spins having comparable or lower resonant frequencies (*45*). The treated 100-nm particles show $^{NV}T_1 = 4.23(7)$ ms approaching the bulk limit of ~6 ms (*46*). The long $^{NV}T_1$ is favorable for achieving high degree of optical pumping in NV ensembles, as it leads to minimal polarization losses from the longitudinal relaxation during long laser pulses (i.e., laser pulses from a few hundreds of microseconds to 1 ms long). Last, although AO and TAC might provide a different balance of functional groups on the surface, this (possible) difference does not seem to affect the

Table 1. Summary of sample properties. P1, NV concentrations, and NV relaxation times are determined by X-band EPR. The T_2 time of NV is measured by Hahn echo ($\pi/2 - \pi$) in pulsed EPR, and the T_1 time is obtained by fitting the decay of the echo-detected NV signal following a laser pulse. The ^{13}C hyperpolarization is characterized by the buildup with the time T_{pol} and the enhancement ϵ_{13C} at the polarization field ($B = 0.287$ T), after combining several approaches for signal improvement (see text and Table 2).

Particle size	P1 density	NV density	$^{NV}T_{2,Hahn}$	$^{NV}T_1$	T_{pol}	Enhanc. ϵ_{13C}
2 μm	39(2) ppm	8.2(5) ppm	2.6(1) μs	3.82(4) ms	34(2) s	1500
100 nm	18(1) ppm	3.4(2) ppm	2.7(1) μs	4.23(7) ms	32(5) s	940

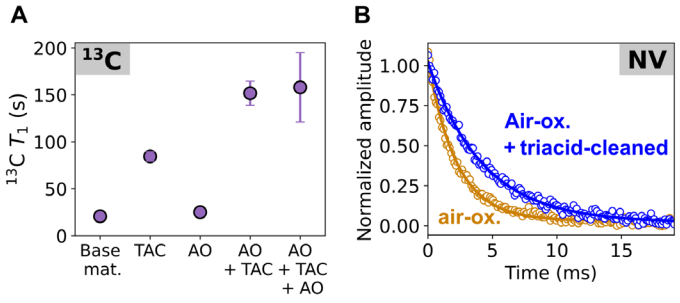

Fig. 1. Improving the spin longitudinal relaxation times of ^{13}C and NV in nanodiamonds (100 nm) by surface treatment. (**A**) Evolution of the $^{13C}T_1$ measured in NMR ($B = 7.05$ T) following treatments of the base commercial material: air oxidation (AO), triacid cleaning (TAC), or combinations (AO + TAC and AO + TAC + AO). Both combinations lead to an about sevenfold improvement over the relaxation time in the original material. (**B**) For the electron-irradiated and annealed sample, containing NV, comparison of the $^{NV}T_1$ taken on the $m_S = 0$ to +1 transition at $B = 0.24$ T, following application of a laser pulse. Solid lines are exponential decay fits, providing $^{NV}T_1 = 2.20(3)$ ms and 4.23(7) ms following the AO and the combined (AO + TAC) treatment, respectively.

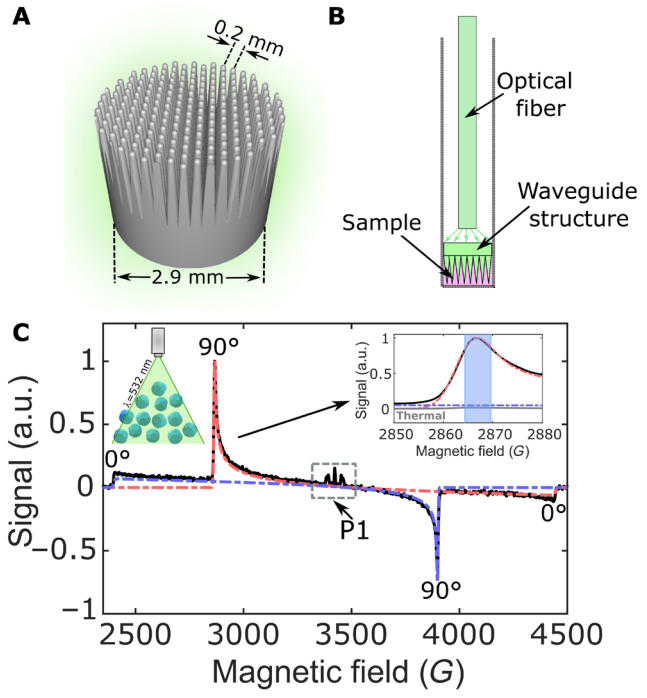

Fig. 2. Description of the microphotonic structure used for illumination. (**A**) Representation of the three dimensionally printed microphotonic structure. (**B**) Schematic illustration of the structure inside the sample tube in the configuration providing optical access to the ensemble of micro- or nanoparticles. (**C**) Pulsed X-band EPR spectrum under illumination for the sample of 2-μm particles. The experimental data (solid black line) was acquired by echo detection following a 700-μs laser pulse using the microwave frequency $\nu = 9.59$ GHz. Dashed red and blue lines are simulated spectra for the two separate spin transitions of NV fitting the experimental spectrum (see section S3.1 for the description of the model used in the simulation). The resonance positions for NV having their axis either aligned (0°) or perpendicular (90°) to the magnetic field locate at the spectrum extremities and on the intense peaks, respectively (as indicated). Besides NV, the P1 spectrum appears in the central part. The right inset shows a zoom on the low-field peak of the optically polarized spectrum and its comparison to the acquired thermal signal (gray), showing here an 85-fold enhancement with illumination. The shaded blue area in the right inset highlights a region corresponding to a range of $\Delta = (2\pi)15$ MHz width in the frequency domain, in which transitions for about 4% of all NV are addressed. a.u., arbitrary units.

longitudinal relaxation, as visible from Fig. 1A. After applying again AO (AO + TAC + AO), no detectable change in $^{13C}T_1$ is observed.

We turn our attention to the process of NV initialization by optical pumping, which is yet another prerequisite to performing (efficient) hyperpolarization. To monitor this process, we use again EPR. In addition to being a valuable tool for determining the concentration, T_1 and T_2 times of NV, EPR allows precise tracking of the redistribution of the NV spin state populations under illumination (*47*). Although EPR spectra of optically polarized NV ensembles in powder samples have been reported (*37*, *48*), performing homogeneous illumination of NV in macroscopic quantities of micro- and nanodiamond remains a challenge, owing to the strong light scattering created by the difference in refractive index between the diamond ($n = 2.4$, at 532-nm wavelength) and its surroundings. To overcome this issue, we couple light into a structure of closely packed waveguides forming an array, in which the diamond powder is embedded together with a solution of ethyl cinnamate acting as buffer between the structure and the diamond, as visible in Fig. 2 (A and B) (details of the illumination protocol are available in Materials and Methods). When illuminating a medium that strongly scatters light, the incoming intensity typically confines into a thin layer below the surface. Using the structure in Fig. 2A aims at improving the homogeneity of illumination, by enhancing the surface area of the sample accessible to the incoming light.

Figure 2C shows the NV spectrum measured with pulsed EPR for the 2-μm particles, using the microstructured waveguide array for illumination with green light (532 nm). The spectrum shows a broad structure, spreading equally on each side of the $g \sim 2$ electron resonance field (on which the signal from P1 centers is centered as well). Considering the large value of the zero-field splitting for NV ($D = 2.87$ Hz), the important inhomogeneous broadening arises in powder samples as the axis of NV within randomly oriented diamond particles has uniform distribution across the complete solid angle. In the dark, the spectrum has a characteristic structure, known as the Pake doublet (*49*), showing two intense positive peaks, corresponding to NV being oriented perpendicular to the magnetic field (*48*, *50*). Under illumination (Fig. 2C), the NV spectrum exhibits positive enhancement in the low-field region and negative enhancement in the high-field part (thus, a zero-crossing near the $g = 2$ resonance). These changes result from the redistribution of populations in the NV ground spin state, here induced by optical pumping. In EPR, the signal scales with the difference in population $(\Delta\rho)_{NV}$ between the two states involved in the spin transition. Thus, by measuring in a chosen spectral region in the dark and comparing the signal to that observed under illumination, the population difference ratio $(\Delta\rho)_{NV} / (\Delta\rho)_{NV,dark}$ can be estimated (section S3.3). In the spectral region in Fig. 2C in which the highest spectral intensity is attained, that is at the low-field peak ($B \approx 0.287$ T), we determine $(\Delta\rho)_{NV} / (\Delta\rho)_{NV,dark} = 46$ and 61, following a 400-μs laser pulse (used later on for NV initialization), for the samples containing 2-μm and 100-nm particles, respectively (fig. S11). With the 100-nm particles being more efficient light scatterers, the mass to be exposed to the laser beam was decreased twofold to keep similar illumination conditions. Considering that the signal intensity in the dark is

governed by the Boltzmann statistics, the absolute population difference is estimated as $(\Delta\rho)_{NV} \approx 3\,\%$ as detailed in section S3.3 (2.4 and 3.2% for the 2-μm and 100-nm particles, respectively). We note that the improvement in NV spin polarization achieved by the waveguides in the structure shown in Fig. 2A is estimated to be by a factor of 3.3, compared to illumination without these waveguides (see fig. S9 for the comparison).

We now focus on the DNP sequence used for NV-^{13}C polarization transfer. Considering that the NV spectrum spans over an extended spectral range (Fig. 2C), corresponding in the frequency domain to over several gigahertz, it appears essential to carefully select the protocol for NV-^{13}C polarization transfer and of utmost importance to look for DNP sequences offering a high degree of robustness to existing parameter inhomogeneities. First, the polarization transfer sequence should reduce the impact of the strong spectral broadening, by working over a wide range of frequency detunings for NV. Second, efficient operation in the presence of Rabi drive imperfections is also desired to alleviate inhomogeneities in the microwave (MW) field or in the NV transition dipole (section S9.3). In this work, we consider the PulsePol sequence, represented in Fig. 3A (*40*), and its variant, shown in Fig. 3B (*51*). As it was noted in (*40*), PulsePol shows a notable difference to the integrated solid effect (ISE) sequence, which was first introduced by Henstra *et al.* (*12*), later used in microdiamonds (*36*, *37*). PulsePol (or its variant) uses discrete pulses, while the ISE exploits the dynamics of the electron-nuclear transitions occurring during a long, continuous pulse (*52*, *53*). With PulsePol, the peak microwave power determines the NV spectral range (Δ_{pol}) in which NV-^{13}C polarization transfer is effective, that is $\Delta_{pol} \sim \Omega_1$ where Ω_1 is the Rabi frequency for NV. This property brings some benefits with respect to the speed of polarization: In the range covered by Δ_{pol}, the NV are addressed in parallel, while sequences such as the ISE manipulate them sequentially, by action of a frequency (or field) sweep. Working with a 40-W microwave amplifier guarantees in our system a Rabi frequency $\Omega_1 = (2\pi)10.5\,\mathrm{MHz}$ for NV, correspondingly, Δ_{pol} remains low in comparison to the (several gigahertz) width of the full NV spectrum. We choose to drive the centers that are oriented at 90° to the magnetic field. This allows enhancing the fraction that is participating to the polarization dynamics, due to the larger solid angle that is covered along the equator of a sphere. For these NV, we choose to drive the transition that shows the highest polarization enhancement under illumination, that is the low-field peak, visible at $B = 0.287\,\mathrm{T}$ in Fig. 2C. The protocol for hyperpolarization is represented in Fig. 3. It consists in repeating the cycle of consecutive laser pulse initialization and microwave driving to gradually build up polarization for the ^{13}C spins.

For improving the robustness properties of PulsePol, a possibility is to use the variant in Fig. 3B from Tratzmiller *et al.* (*51*), which relies on alternative pulse phase definitions compared to the original sequence in Fig. 3A (hence, the label "phase-offset PulsePol"). Besides the increased robustness against frequency detuning, which could be verified by performing ^{13}C hyperpolarization in single crystal diamond (section S6.1), the phase-offset variant is also expected to mitigate inhomogeneities in the Rabi drive to a degree comparable to what is achieved in the standard PulsePol. The resonance condition for polarization transfer can be expressed similarly in both sequences as $\tau = \frac{n\pi}{\omega_I}$ where τ is the length of the six-pulse block (Fig. 3) and ω_I is the Larmor frequency of the target nuclear spins. However, the phase-offset PulsePol has half-integer resonances (see section S6.2), contrasting with the odd-integer resonances $n = 1,3,5,7$, etc., as in the original PulsePol.

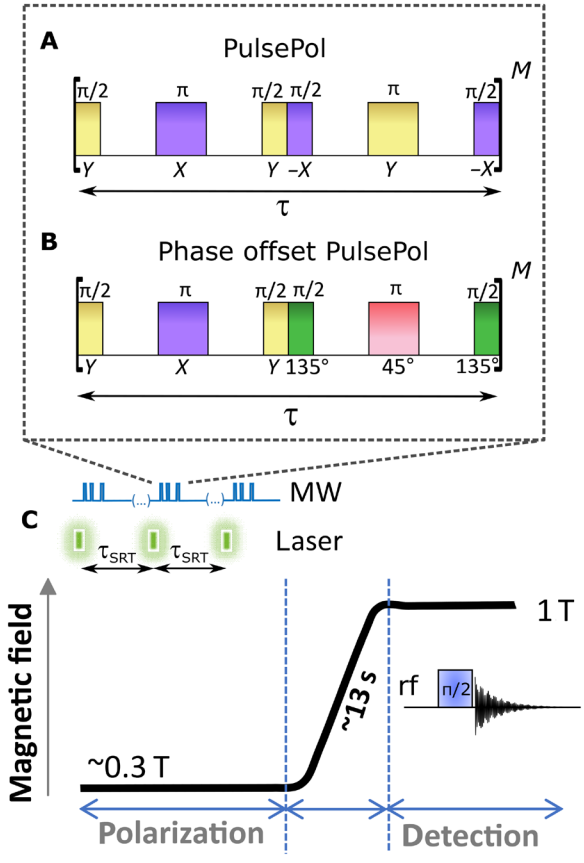

Fig. 3. Sequences and timings. (**A**) Conventional PulsePol sequence and (**B**) phase-offset variant. Both the sequences in (A) and (B) include equal delays between the π and π / 2 pulses. By adjusting these waiting times, one varies the interval τ (length of the six-pulse block), which determines the resonant condition for polarization transfer. The represented pattern is repeated *M* times, so that $M \times \tau$ is the duration of the interaction with the nuclear spins. (**C**) Illustration of the hyperpolarization protocol. One polarization cycle consists in performing NV initialization by a laser pulse and polarization transfer using one of the sequences in (A) and (B). The cycle is repeated at regular intervals (with a period τ_{SRT}) to build up nuclear polarization. For NMR detection, the magnetic field is ramped up to 1 T, which takes about 13 s, and the ^{13}C signal following the application of a radio frequency (rf) pulse is acquired in situ.

Considering NV oriented at about 90° to the magnetic field has consequences on the dynamics during the application of the DNP sequence. The magnetic field tilt leads to forbidden transitions involving both the NV electronic spin and the ^{14}N nuclear spin (illustrated in fig. S18), which can be seen as a consequence of the magnetic field breaking the C_{3v} symmetry of the NV (thus, the forbidden transitions occur also at tilts lower than 90° and vanish only in the 0° case). A commonly observed effect of these transitions is the so-called electron spin echo envelope modulation on NV (*54*). In the context of DNP, however, the forbidden transitions open a channel for NV relaxation, which does not participate to the build-up of polarization among ^{13}C nuclear spins. Owing to the approximately megahertz strength of the NV-^{14}N hyperfine coupling terms (*55*), higher than the typical ~100-kHz strength of NV-^{13}C coupling

from the dipolar interaction at 1.1% ^{13}C (*53*), it is important to minimize some effects of the NV-^{14}N interaction to preserve the slow dynamics of ^{13}C nuclear spin polarization during the DNP sequence. This should be taken into account when choosing the resonance condition in PulsePol. In the absence of NV-^{14}N interaction, the $n = 3.5$ resonance condition of the phase-offset PulsePol is expected to offer better performance [similarly to the original PulsePol in Fig. 3A, where the $n = 3$ resonance is known to be optimal (*40*)]. However, our results evidence an improvement in the ^{13}C polarization by a factor of 1.7 when using rather the $n = 4.5$ resonance. Simulations at our magnetic field ($B = 0.287$ T) demonstrate that the τ-value corresponding to the $n = 4.5$ condition is quasi-optimal for refocusing the NV-^{14}N interaction and thereby avoiding partial inhibition of the polarization transfer to ^{13}C, while the $n = 3.5$ resonance is non-optimal (see section S6.2 for the experimental comparison of the resonances, the description of the NV-^{14}N interaction, and simulations). We therefore use the $n = 4.5$ resonance condition, but note that it could turn less advantageous at other magnetic fields, as it would correspond to a different τ-value due to the change in ^{13}C Larmor frequency and as the dynamics of the ^{14}N spin is field dependent. In this case, one could potentially use a variant of PulsePol with another setting of the pulse phases to obtain more favorable resonances (*51*) while keeping sequence robustness properties comparable to the standard PulsePol.

Even when using the more robust sequence variant in Fig. 3B, the bandwidth Δ_{pol} remains low in comparison to the width of the full NV spectrum. Thus, it is beneficial to implement strategies for increasing further the number of NV contributing to the polarization transfer process. We now discuss such additional methods and optimize them by detecting the hyperpolarized signal in the 2-μm sample, before applying them as well to the 100-nm nanodiamonds.

The first method consists in replacing the individual rectangular pulses by "composite" versions to provide further robustness to frequency detuning. We consider composite pulses described by Shaka and Pines (*56*), which are built by adding "sidebands" of alternating phases around a central rectangular pulse. In this work, the pulses by Shaka and Pines are refined by the introduction of waiting times and then numerically optimized to improve their robustness. In our conditions $\Omega_1 = (2\pi)10.5$ MHz, we determined that the simplest (two-sideband) version of the pulses leads to efficient operation of PulsePol in the range $\Delta_{pol} = (2\pi)15$ MHz (see section S6.3 for description of the pulses optimization and sequence robustness properties). Owing to the asymmetric shape of the Pake doublet peak, the magnetic field was offset by a few gauss to maximize the number of addressed NV, as shown in inset of Fig. 2C, where we have represented a spectral region corresponding to the 15 MHz of excitation width. We estimate that this spectral region covers approximately a fraction of 4% of all centers, corresponding to NV oriented with a tilt (θ) from the magnetic field such that $|\theta - 90| \lesssim 2.5°$ (see section S9.2). In Fig. 4C, the hyperpolarized ^{13}C signals obtained using the standard and the optimized two-sideband pulse are compared, showing an improvement by about 30% compared to the latter (setting parameters such as the repetition number $M = 68$, and the sequence repetition time $\tau_{SRT} = 1.5$ ms, which appeared to be optimal; see section S6.4). We note that the duration of the pulses is constrained by the chosen PulsePol resonance condition, as it is visible from Fig. 3, the length of the π pulse should not exceed $\tau/4$. This restricted us from using "higher-order" versions (i.e., with more than two sidebands) of the pulses, although these are predicted to be more efficient. These would be within reach using a more powerful amplifier.

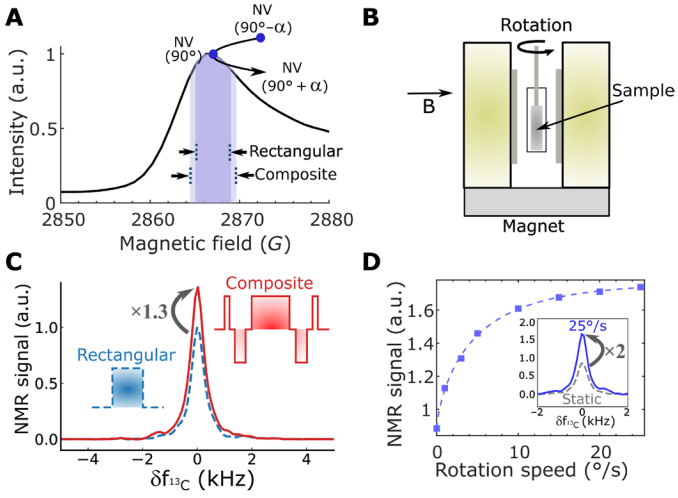

Fig. 4. Strategies for improved polarization transfer efficiency. (**A**) NV EPR spectral line. The microwave excitation bandwidth is extended by using composite pulses instead of rectangular, and slow sample rotation enables a larger number of NV with various orientations to the magnetic field to pass through the bandwidth. (**B**) Illustration showing the orientation of the rotation axis in the experimental setup. (**C**) Comparison of the hyperpolarized ^{13}C NMR signals obtained using rectangular and composite pulses. (**D**) Hyperpolarized ^{13}C NMR signals obtained with sample rotation at different speeds. The dashed line is a stretched exponential fit as described in the text, yielding parameters $\omega_{r,0} = 4.9(5)°/s$ and $\beta = 0.74(6)$ as the stretch exponent. Acquisitions represented on this figure were taken on the 2-μm sample.

As an additional approach for enhancing the signal, we implemented slow sample rotation, around an axis perpendicular to the magnetic field (Fig. 4, A and B). This allows cycling through different NV subsets, as those defined by the excitation region of PulsePol will be progressively replaced, upon rotation, by NV of different initial orientation. The slow sample rotation implemented as in Fig. 4B will bring the axis of any NV to a direction orthogonal to the magnetic field, ensuring that its spin transitions meet the 90° resonances. We rotate at speeds up to 25°/s , the maximum allowed by our rotation stage, and obtain an increase in the ^{13}C signal that is twofold at the maximum velocity (Fig. 4D). This suggests that switching regularly the subset of NV that is addressed by the polarization transfer sequence is favorable, compared to using continuously the same subset.

We can understand this observation from the dynamics of the ^{13}C polarization buildup. Without applying rotation, the increase of signal with the polarization time follows a so-called stretched exponential function $s(t) = A\left(1 - \exp\left\{-\left(\frac{t}{T_{pol}}\right)^{\beta}\right\}\right)$, with $T_{pol} = 29(4)$ s and $\beta = 0.70(8)$ (fig. S14). Consequently, efficient polarization occurs at short times, $s(t) \sim \left(\frac{t}{T_{pol}}\right)^{\beta}$, as $\beta < 1$. It was previously observed that (*57*): (i) Initially, the buildup occurs because of direct polarization of ^{13}C spins from NV or spin diffusion on short length scales, while at longer times, it acquires (slower) dynamics affected by the less efficient spin diffusion at longer scales; and (ii) the NV acts in its very close surroundings, as a relaxation sink for nuclear spins shortening their T_1. Here, we exploit this dynamic to benefit from the efficient polarization creation regime at short times (by

rotating the sample) but still address distant ^{13}C spins, with a long nuclear T_1. From Fig. 4D, increasing the rotation speed (ω_r) first enhances steeply the signal $s(\omega_r)$, which reaches an apparent saturation at high speeds. This behavior can be fitted as $s(\omega_r) = s_0 + A\left(1 - \exp\left\{-(\omega_r/\omega_{r,0})^{\beta}\right\}\right)$, that is a stretched exponential, from which $\omega_{r,0} = 4.9(5)°/s$ is extracted and $\beta = 0.74(6)$. The stretched exponential behavior reminds of that of the polarization buildup. It is instructive to consider the overall rotation angle during the characteristic time of nuclear polarization buildup, that is, $\omega_r T_{pol}$. At a speed $\omega_r \approx \omega_{r,0}$, one has $\omega_r T_{pol} = \omega_{r,0} T_{pol} = 142(20)°$, which is close to the condition when half a turn (180°) is performed during T_{pol}. Thus, the important signal increase provided by rotation in the range of speed $\omega_r < \omega_{r,0}$ occurs as more of the different NV subsets are progressively being involved in the polarization transfer, until all NV participate (at $\omega_r \approx \omega_{r,0}$). At the maximum speed (25°/s), we measure a polarization buildup time $T_{pol} = 34(2)$ s comparable to that in the static sample. As the buildup dynamic is ultimately determined by the relaxation properties (T_1) of the spins that are being polarized, our observation indicates that ^{13}C populations with comparable T_1 are being addressed in the experiments with and without rotation. Because the signal is maximally increased by rotation (25°/s), we use this setting in the rest of our experiments.

In the experiments, the number of repetitions $M = 68$ (M is defined in Fig. 3) was used in PulsePol, based on the dependency of the detected ^{13}C signal on M (fig. S22). The latter shows, first, an increase in the nuclear polarization with the repetition number at low repetition numbers and, second, evidences a saturation regime at $M \gtrsim 55$ ($M\tau \gtrsim 40\,\mu s$), to which the value $M = 68$ belong. While the initial rise in the signal occurs as a higher repetition number gives the possibility of polarizing directly nuclear spins further away from the NV, thus enhancing the overall efficiency of hyperpolarization, the saturation is likely related to the limit set by the NV decoherence, as the latter leads to a decrease of the polarization transfer efficiency at long driving times. The microwave driving of the polarization sequence, particularly the fact that it differs from simple refocusing by Hahn echo, is important here as, considering the coherence time measured by Hahn echo (Table 1), one would expect a maximum ^{13}C signal to be reached only after $3T_{2,Hahn} \approx 8\,\mu s$. Instead, applying the DNP sequence ensuring polarization transfer to ^{13}C leads also to coherence prolongation, as it decouples the NV from low frequency components of the magnetic noise. Therefore, $T_{2,PP}$, the coherence time under PulsePol, is predicted to obey $T_{2,PP} > T_{2,Hahn}$, which explains that nuclear signal improvement is seen, even for microwave driving durations exceeding $3T_{2,Hahn} \approx 8\,\mu s$.

Combining the above-mentioned strategies, each of the factors in Table 2 independently enhances the signal. The resulting ^{13}C hyperpolarized signals are represented in Fig. 5. The enhancements over the ^{13}C thermal signal at the polarization field are $\epsilon_{13C} = 1500$ for the 2-μm particles and $\epsilon_{13C} = 940$ for the 100-nm particles, thereby demonstrating hyperpolarization using an optically pumped color center at ambient conditions in diamond nanoparticles (< 200 nm). It is worthwhile to remark the speed at which the signal in Fig. 5 is achieved, i.e., running the DNP protocol for 5 min, which

Table 2. Estimated contributions to the overall hyperpolarization gain. For factor (a), the gain applies to the 100-nm nanodiamonds and is estimated from the ^{13}C T_1 times shown in Fig. 1A, measured at $B = 7.05$ T. The ^{13}C T_1 time typically affects linearly the hyperpolarized signal level (longer T_1 provides longer polarization buildup time). For (b), the gain corresponds to the NV spin polarization enhancement provided by using the microphotonic structure to ensure more uniform illumination. For factors (c) to (e), the gain is determined directly from ^{13}C hyperpolarization (see also Fig. 4). The improvement (e), specifically, refers to setting the τ-delay ($\tau = \frac{n\pi}{\omega_l}$) to $n = 4.5$ to reduce the adverse effect of the NV-^{14}N interaction at the present magnetic field, instead of using the lower order resonance, $n = 3.5$, typically chosen in the PulsePol sequence in Fig. 3B.

Factor	Improvement source	Mitigated effect	Estimated gain
(a)	^{13}C T_1 time	Surface-induced T_1 relaxation	×7
(b)	Sample illumination	Light scattering by the particles	×3.3
(c)	Sample rotation	Inhomogeneous broadening of NV	×2
(d)	Composite pulses	Inhomogeneous broadening of NV	×1.3
(e)	PulsePol *n*-adjustment	NV-^{14}N dynamics	×1.7

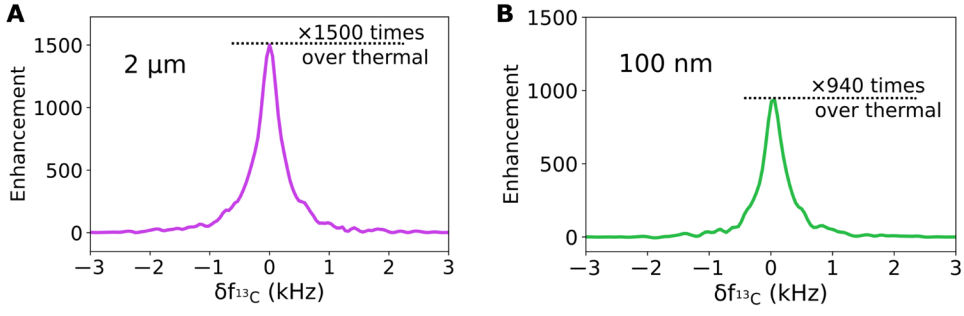

Fig. 5. ^{13}C hyperpolarized signals. ^{13}C NMR signal obtained after 5 min of hyperpolarization for 2-μm (**A**) and 100-nm (**B**) diamond particles. The spectra intensities are normalized by the ^{13}C thermal signal at the polarization field (0.287 T), showing enhancements of 1500 and 940 times in (A) and (B), respectively.

is sufficient to reach the maximum of the buildup for both samples. We measured 34(2) s and 32(5) s as buildup times (T_{pol}) in the 2-μm and 100-nm particles, respectively. Relaxation times of 142 ± 16 s and 116 ± 16 s govern the decay of the hyperpolarized signal at 1-T magnetic field (section S4.1). A stronger enhancement is observed in the 2-μm sample. In the simplest description, for samples of similar polarization buildup times, we expect the enhancement factor to scale with the efficiency of NV initialization and their density ([NV]), so that $\epsilon_{13C} \propto (\Delta\rho)_{NV} \cdot [NV]$. Thus, from the NV concentrations (Table 1) and from the determined $(\Delta\rho)_{NV}$, one would expect $\epsilon_{13C}^{2\,\mu m} / \epsilon_{13C}^{100\,nm} = \frac{0.024}{0.032} \cdot \frac{8.2\,ppm}{3.4\,ppm} = 1.8$, which is close to what we observe, i.e., $\frac{1500}{940} = 1.6$. To explain the small discrepancy between 1.8 and 1.6, we would like to point to a possible role of NV-NV interactions, which should result in faster NV decoherence during the application of PulsePol (shorter $T_{2,pp}$) in the case of dense NV ensembles. Although this is outside of the scope of the present work, it might be beneficial, when working with extremely dense NV ensembles, to apply sequence modifications for refocusing the dipole-dipole interaction between the different NV (*58*).

Our findings allow discussing the spatial distribution of the polarized ^{13}C spins, which is of fundamental interest. Considering the natural isotopic content (1.1%) of ^{13}C in our samples, the spread of polarization by spin diffusion is predicted to follow the coefficient $D = 6.7 \times 10^{-15} cm/s^{-2}$ (*35*). Taking into account our buildup times, $T_{pol} \sim 30$ s, we obtain as diffusion length $l \sim \sqrt{DT_{pol}} = 4$ nm. For randomly distributed defects, the nearest-neighbor distance is $r_{NN} = 0.55 n^{-1/3}$, where n is defect density. We calculate that the NV concentrations in Table 1 correspond to comparable distances, $r_{NN} = 4.9$ nm and $r_{NN} = 6.5$ nm, for the 2-μm and 100-nm samples, respectively. In our samples, spin diffusion, therefore, leads the polarization to reach most parts of the diamond lattice between the different NV, which is in line with conclusions drawn previously in the context of single crystal experiments (*59*).

To investigate the benefits specifically provided by our DNP sequence, we applied the ISE instead of PulsePol. As a conservative comparison, keeping the sample rotation at 25°/s, we consider a frequency sweep over a 50-MHz-wide range of detunings, that is, addressing a higher fraction of NV than in our implementation of PulsePol. Nevertheless, with the ISE, the obtained ^{13}C polarization is about threefold lower, as we obtain $\epsilon_{13C} = 570$ instead of $\epsilon_{13C} = 1500$ for the sample in Fig. 5A (section S7). This points to a substantially lower efficiency of the ISE in terms of the nuclear polarization it achieves on a "per NV" basis, i.e., for a given fraction of the spectral range. Although this discrepancy can occur from a combination of factors, in our analysis, a particular one stands out. PulsePol made it possible to minimize the losses of NV polarization due to the NV-^{14}N interaction, for the 90° NV orientation, through the choice of the resonance condition. In the context of the ISE, however, the hyperfine interaction to the ^{14}N plays out differently. Considering the dynamics of the ISE, the possibility exists that NV exchanges its polarization to the ^{14}N during the microwave frequency sweep, by excitation of one of the forbidden transitions, before the condition for NV-^{13}C polarization transfer is met (see section S7.2 for a detailed description). Thus, the consequences of the interaction to ^{14}N, which could be mitigated with PulsePol by choosing a specific resonance condition, can substantially hamper the transfer of polarization to ^{13}C in the case of the ISE. Last, in our system, extending the sweep range above 50 MHz yields only a moderate improvement ($\epsilon_{13C} = 650$ for a 200-MHz width); however, the resonator bandwidth does influence the polarization transfer by the ISE (section S7).

Owing to the small fraction of time that our implementation of PulsePol takes in the full polarization cycle, room exists for the optimization of PulsePol. To obtain the signal in Fig. 5, the sequence in Fig. 3B was used with a duration $M\tau \approx 50\,\mu s$, which is much shorter than the laser initialization pulse (400 μs), the repetition interval ($\tau_{SRT} = 1.5$ ms) and the decay of NV polarization ($^{NV}T_1 >$ ms). There exist intervals, both between the pulses and after, where the PulsePol sequence could be applied at different carrier frequencies. In future developments, this could be considered for improving our bandwidth (Δ_{pol}) and thus enhancing further the hyperpolarized signal (section S8).

Last, although our efforts were focused on NV in the diamond material, our approach can be extended to centers with optical pumping capability in different host lattices. Spectral broadening induced by the anisotropy, which we observe for NV, will occur similarly for other known defects, such as pentacene in naphthalene crystals or the divacancy in silicon carbide ($S = 1$).

DISCUSSION

We highlight that attaining the high ^{13}C polarization levels evidenced by the NMR signals in Fig. 5 is the payoff from combining improvements from different sources (listed in Table 2). Besides the sevenfold prolongation of the nuclear T_1 by combining the AO and acid cleaning treatments, we applied more uniform illumination by enhancing the surface of the sample accessible to the 532-nm light using the microphotonic structure in Fig. 2. The DNP sequence (PulsePol), which we apply on an ensemble of randomly oriented NV, was adjusted to strongly mitigate the, otherwise, unfavorable effect of the NV-^{14}N dynamics, bringing a 70% improvement. The addition of composite pulses brought a 30% improvement in the hyperpolarized signal and slow sample rotation, which leads to more NV being involved into the polarization transfer process, allowed enhancing the signal further twofold. Using the PulsePol sequence as part of this protocol enhances the signal threefold in comparison to using the ISE over a comparable spectral range.

Let us consider from the enhancement factors in Fig. 5 the absolute nuclear polarization, defined as $p_{13C} = \frac{N_\uparrow - N_\downarrow}{N_\uparrow + N_\downarrow}$ where $N_\uparrow$ and $N_\downarrow$ are the populations of the two Zeeman spin states of ^{13}C. The value of p_{13C} constitutes a figure of merit that is independent on the detection field. Applying the enhancement values observed in Fig. 5 to the Boltzmann population, $p_{13C,thermal} \approx \frac{\hbar\omega_I}{2k_B T} = 2.52 \times 10^{-7}$ (room temperature, 0.287 T), one obtains 0.038 and 0.024 % as p_{13C} for the 2-μm and 100-nm powder samples, respectively. We discuss this outcome in the light of the work of King *et al.* (*33*), who used single crystal diamond with similar bulk material properties as our powders (electron-irradiated type Ib diamond). In that work, after performing DNP at 0.42-T magnetic field, the value of 6% of absolute ^{13}C polarization was observed, which exceeds by a factor of 160, our best result (2-μm particles). We attribute this discrepancy to the combination of several factors as follows. First, King *et al.* performed NV-^{13}C polarization transfer using NV aligned to the magnetic field in single crystal diamond, which represents the ideal conditions for generating high electron spin polarization by optical pumping. Although the precise enhancement of NV signal by

illumination was not reported, it is common to reach, under such conditions, a population difference between the optically pumped ($m_S = 0$) and any of the optically depleted ($m_S = \pm 1$) states that obey $(\Delta\rho)_{NV} > 30\%$ (*47*), i.e., improved more than 10-fold compared to our powders. We note that, besides the absence of light scattering, the suppression of spin state mixing for this NV alignment also likely plays a role in the improvement on $(\Delta\rho)_{NV}$ (which accounts for a factor of about 2, according to the model fitting our powder spectrum, described in section S3.1). Second, NV in single crystal belongs to four homogeneously oriented subsets. This enables working conveniently with a fourth of all NV (25%), which yields, in comparison to our powder, another factor of $25/4$ (≈ 6). Thus, it is expected to observe > 60 increases in the enhancement factor in single crystal, compared to powder in the present conditions of our work.

For applications, in particular, considering the use of nanodiamonds as MRI tracers, increasing the nuclear polarization levels beyond that obtained with our current approach is desired. For diamond particles with natural abundance of ^{13}C, it has been shown that values of $p_{13C} = 0.2$ to 1% (that is a factor of 10 to 20 above our results) enable MRI acquisitions with a good signal-to-noise ratio (SNR), i.e., comparable to the modality of using hyperpolarized ^{13}C-pyruvate for metabolic imaging (*18*). From the considerations of the limiting factors, we suggest possible ways to reach such levels. We expect that combining the application of the sequence at different frequencies (multiplexing) and pulse shaping would enable increasing the width of the spectral range Δ_{pol} to 100 MHz, which corresponds to about 16% of NV (section S8). Better initialization of NV could be achieved through the use of higher laser intensities; however, in our experimental configuration, the laser intensity that can be applied was limited by sample heating. Temperature elevation in our micro- and nanodiamonds was estimated from resonance shift in the NV EPR spectrum, to be 51 K for the 2-μm particles and 24 K for the 100-nm particles (section S3.2). We used, for both samples, a configuration in which the diamond particles are densely packed, which favors localized heating. Better heat dissipation would be attained using an illumination geometry that allows also for the sample to be sparsely dispersed, in a gel or a liquid (possibly still using microstructured waveguides to counter light scattering). Although the realization might present some challenges, this could be combined with some designs already used for efficient cooling (*60*).

Dispersion in a fluid might promote particle reorientation by thermal motion, which has been a proposed alternative to mechanically rotating the sample during the application of the polarization sequence (*52*). However, the fluid viscosity, which determines the tumbling rate for nanodiamonds of a given size, might need to be carefully controlled as the reorientation dynamics should not make the nanodiamonds depart strongly from their orientation while NV is being driven by microwave. For a particle with $r = 80$ nm as hydrodynamic radius, using the Stokes-Einstein-Debye relation for the rotational diffusion coefficient, $D_r = k_B T / 8\pi\eta r^3$ in glycerol of dynamic viscosity $\eta = 1.4\,\mathrm{Pa \cdot s}$ at room temperature ($T = 293$ K), one has $D_r = 0.22\,\mathrm{s}^{-1}$. In the conditions of our experiment, the region of efficient polarization transfer lies within a $90 \pm 2.5°$ angle range from the magnetic field direction. Considering the root mean square diffusion angle $\delta = \sqrt{2D_r t}$, thermal motion will drive the nanodiamond out of this orientation range after a time $t \approx 4.3$ ms. The "residence time" is longer by two orders of magnitude than the duration of application of PulsePol in our protocol ($M\tau \approx 50\,\mu$s); thus, microwave driving with PulsePol will remain effective. The full polarization transfer cycle, including initialization, microwave driving, and waiting time, takes 1.5 ms and, therefore, could be applied three times, on average, before the nanodiamond moves to a less favorable orientation. This number of repetitions lies below what we established by mechanical rotation (>130 polarization cycles, corresponding to >200 ms); however, the viscosity of the fluid could be varied, e.g., by moderate cooling, to make the number of repetitions comparable. Our findings suggest that slow reorientation, which ensures that most nanodiamonds enter the bandwidth during the nuclear T_1 time, is already sufficient to provide a substantial improvement in the hyperpolarized signal.

Turning to the polarization decay time ($^{13C}T_1$), it can be seen from the above-reported values that the decay in our samples occurs much faster than what has been reported for ultrapure single crystals (*21*), which we attribute to the high concentration of paramagnetic species (P1, NV, and others), providing relaxation channels via flip-flops or via their own T_1 process (*59*). We now discuss consequences in terms of applications and possible routes for material development.

Despite being low by the standards of ultrapure diamond, the $^{13C}T_1$ times that we observe are expected to be sufficient for some applications. A possible follow-up experiment to our work would consist in using "core-shell" particles, in which it is possible to obtain comparable T_1 times for a highly (~100% ^{13}C) isotopically enriched shell, overgrown on naturally abundant nanodiamonds containing NV, similar to the material used in the current work (*61*). As originally reported, this would enable mediating spin polarization transferred from NV in the "core," toward the surface, using spin diffusion in the enriched shell. These particles present an exciting opportunity for advancing toward the hyperpolarization of external substances. By using cross-polarization sequences between nuclei within the diamond and those in a target compound, it may become feasible to transfer polarization to solids or highly viscous liquids. Conversely, for conventional liquids, polarization transfer could occur via the nuclear Overhauser effect [however, the optimization of this process might require considering specific fluid dynamics at the nanoparticles' surface; (*16*)]. Besides, if NV initialization and microwave driving can repeatedly be applied, such nanodiamonds would constitute a replenishable source of polarization. In particular, this could be of direct interest for NMR detected in situ. Nevertheless, the ability for spin polarization to efficiently reach the particles' surface would need to be investigated as, potentially, shorter nuclear T_1 for ^{13}C located in the vicinity of the surface (due, e.g., to dangling bonds) could constitute a polarization loss channel.

For the other envisioned application, using nanodiamonds in MRI as tracers, it must be kept in mind that the ^{13}C polarization must survive while the nanodiamonds diffuse to the location of interest (e.g., tumor), which can be long (*62*). This points to a possible limitation of the material used in the present study, for which the $^{13C}T_1$ restricts the time before detection to a few minutes. An approach for improving the nuclear T_1 consists in performing electron irradiation on a sample with low nitrogen content, with the rationale of keeping the overall content of paramagnetic spins low. This was demonstrated to provide hour-long lifetimes in single crystals while still allowing efficient ^{13}C hyperpolarization (*34*). Recently, long coherence for NV under Hahn echo and dynamical decoupling were observed in milled chemical vapor deposition diamond, suggesting the possibility of producing ~200-nm particles with low magnetic noise levels, comparable to that in high-quality bulk

material (*63*). In smaller particles (100 nm and below), however, one might need to consider as well dangling bonds or impurities in the diamond that are thought to be stabilized as a coproduct of surface irregularities (*29*, *64*). The desired reduction in the number of the surface-related defects in particles of 100 nm and below might require the combination of material engineering for producing particles of near-spherical shape with a smooth surface, and approaches for reduction or passivation of possibly remaining defects.

In summary, combining improvements on the material and in the dynamical nuclear polarization protocol, we demonstrated the hyperpolarization of ^{13}C in diamond particles down to 100-nm size, using the optically pumped NV center as polarization source. In the nanoparticles, the impact of the magnetic noise from surface sources is reduced by combining treatments of AO and TAC, ensuring a long T_1 for the ^{13}C spins. For improved NV initialization, the light scattering by the nanoparticles is mitigated by performing illumination using microstructured waveguides, leading to strong enhancement for the peaks in the Pake doublet spectrum of NV, corresponding to the centers oriented at 90° to the magnetic field. In the PulsePol sequence used for polarization transfer, the resonance condition is chosen to virtually suppress the otherwise unfavorable effects of the NV-^{14}N hyperfine interaction. To reduce the impact of the spectral broadening of NV in powder samples, the PulsePol sequence is further optimized, and slow sample rotation (25°/s) is performed. In contrast with protocols previously used for nanodiamonds (< 200 nm), our approach does not require cryogenic temperatures. The current results establish NV-containing nanodiamonds as a platform for hyperpolarization based on ^{13}C spins at ambient conditions, promising future applications in the fields of sensitive NMR or MRI.

MATERIALS AND METHODS

Diamond powders with ~2-μm and 100-nm median particle size (Pureon AG, type Ib, HPHT, MSY1.5-2.5 and MSY 0-0.2) were used as starting material. To form NV, the samples were electron irradiated with a dose of 3×10^{18} cm^{-2} in a 10-MeV electron accelerator operating under permanent argon flow. The temperature during the irradiation was maintained at 800°C by controlling the dose per pulse and repetition frequency of the accelerator. To clean the surface of diamond particles from graphitic residues, the AO treatment consists in annealing the samples at 620°C for 5 hours in air (*41*). For removing metallic residues, the TAC treatment consists in exposition to a high-concentration three-acid mixture of HNO_3 (40%), $HClO_4$ (70%), and H_2SO_4 (90%) in 1:1:1 proportions, under conditions of 200°C temperature and 6-bar pressure, for ~2 hours. To prepare samples for the hyperpolarization experiment, a mass of 12 mg was used for the 2-μm powder. For the 100-nm sample, 6 mg was used.

The longitudinal relaxation times of ^{13}C nuclear spins shown in Fig. 1A were obtained using a 300-MHz WB NMR system at room temperature and $B = 7.05$ T magnetic field, equipped with an Avance III console (Bruker Biospin GmbH).

Characterization of paramagnetic defect concentrations and their spin properties, as well as the implementation of polarization transfer from NV to ^{13}C nuclear spins, were made with the X-band Bruker Elexsys E580 spectrometer (9 to 10 GHz). The ER-4122-SHQE resonator was used for spin counting using continuous-wave (CW) EPR. The pulsed FlexLine resonator ER-4118X-MD5 with the traveling wave tube (TWT) amplifier from Applied System Engineering Inc. (Model no. 117) served to characterize the NV T_1 and T_2 times.

The microphotonic structure used for sample illumination was manufactured using a commercially available direct laser writing system, using the two-photon-polymerization technique (Photonic Professional GT+, Nanoscribe GmbH, Eggenstein-Leopoldshafen, Germany). We used the resin IP-S (Nanoscribe GmbH, Eggenstein-Leopoldshafen, Germany) because of its excellent optical properties in the visible range and a 10× lens with numerical aperture = 0.3 for fast prototyping progression. The structures were printed on a silicon wafer using the dip-in approach, where the resin acts as its own immersion medium. The slicing and hatching distances were chosen as 5 and 1 μm, respectively, which, although showing visible steps between layers, still produced good quality results. Uncured resin was dissolved and removed by submerging the structure in propylene glycol methyl ether acetate, and cleaning was done by a subsequent bath and rinsing with isopropyl alcohol during which ultraviolet curing was applied to ensure the complete polymerization of all components and to reduce shrinkage. The structure itself comprises a base with a diameter of 2.9 mm, on which a hexagonal pattern of ~200 pillars, each around 1 mm in height, is placed (Fig. 2A). The pillars are truncated cones that are topped by a hemispherical cap. The distance between the revolution axes of neighboring pillars is 200 μm. From the volume in between the pillars and the corresponding surface in contact with the structure ($V = 3.67$ mm^3 and $S = 111$ mm^2, respectively), we calculate, for a sample present in the space between the pillars, $S/V = 30.2$ mm^{-1}. This represents a 17-fold increase in the surface-to-volume ratio compared to the case in which the sample would be simply illuminated through a 2.9-mm-diameter disk, i.e., keeping the same configuration of illumination but removing the structure.

In the sample preparation, the diamond powder was mixed with ethyl cinnamate ($C_{11}H_{12}O_2$), the latter, with a refractive index ($\lambda = 532$ nm) $n = 1.57$, has the following use for index matching: (i) It reduces losses by internal reflection inside the structured array, and (ii) it mitigates further the effects of light scattering by the diamond particles. The mixture of diamond powder and ethyl cinnamate (with a mass equal or lower to that of the diamond powder) provides a viscous fluid, which was placed in a sapphire tube (4-mm outer diameter, Situs Technical GmbH, Wuppertal, Germany), and the waveguide structure was placed on top. As shown in Fig. 2B, an optical fiber (1.5-mm diameter) delivers the illumination.

A 3-W 532-nm diode-pumped solid-state laser from Laserglow Technologies was used and pulsed using transistor-transistor logic modulation. Because of losses, the power at the output of fiber is 1.6 W. The laser pulse length was set to 700 μs when measuring spectra as in Fig. 2 and to 400 μs in the hyperpolarization experiment. Considering the repetition time of 1.5 ms, the 400 μs correspond to an average laser power of 420 mW. At this power, the illumination induces some heating of the samples, which was evaluated to be 51 and 24 K for the 2 μm and 100 nm, respectively (section S3.2).

Nuclear hyperpolarization was performed using the pulsed-ENDOR EN-4118X-MD4 resonator. To address the duty cycle limitations of the TWT amplifier, a 40-W CW solid-state microwave amplifier from AR Deutschland GmbH (40S6G18B 6 to 18 GHz) was used, replacing the TWT. The sequences shown in Fig. 3 were implemented with the Bruker SpinJet AWG. To perform in situ detection of the hyperpolarized ^{13}C NMR signal, we used the radio frequency (rf) coil of the ENDOR resonator. A tank circuit was added outside the resonator for tuning and matching, allowing for detection of NMR signal around the resonance frequency of ^{13}C spins at 1 T ($\nu_{13C} \sim 10.7$ MHz). The NMR signal is detected

using a KEA^2 console (Magritek GmbH) using a 500-W rf amplifier from (BT00500-ALPHA-SA from Tomco Technologies) for pulse amplification.

To obtain the data represented in Figs. 4 and 5A, the hyperpolarized signal was accumulated five times. In Fig. 5B, the signal was accumulated 30 times (owing to the lower sample quantity and enhancement, this allows reaching SNR comparable to the data in Fig. 5A). Acquisition of the ^{1}H NMR signal from a water sample of known volume was used as an intensity reference to determine the ^{13}C signal enhancement values in Fig. 5 (see section S5 for details on the enhancement determination).

The XPS acquisitions described in SM were performed using a Physical Electronics instrument (PHI 5800). The equipment was equipped with a hemispherical electron analyzer, a monochromatic Al Kα x-ray source (1486.6 eV), and a flood gun to prevent sample charging. The spectra were recorded with a pass energy of 93.9 and 29.35 eV for the survey and the high-resolution spectrum, respectively. The XPS spectra were calibrated using the C1s peak as a reference, which corresponds to a binding energy of 284.7 eV.

Supplementary Materials

This PDF file includes:

Sections S1 to S9
Figs. S1 to S29
Tables S1 to S5
References

REFERENCES AND NOTES

1. J. Eills, D. Budker, S. Cavagnero, E. Y. Chekmenev, S. J. Elliott, S. Jannin, A. Lesage, J. Matysik, T. Meersmann, T. Prisner, J. A. Reimer, H. Yang, I. V. Koptyug, Spin hyperpolarizationin modern magnetic resonance. *Chem. Rev.* **123**, 1417–1551 (2023).
2. P. Nikolaou, B. M. Goodson, E. Y. Chekmenev, NMR hyperpolarization techniques for biomedicine. *Chem. A Eur. J.* **21**, 3156–3166 (2014).
3. Z. J. Wang, M. A. Ohliger, P. E. Z. Larson, J. W. Gordon, R. A. Bok, J. Slater, J. E. Villanueva-Meyer, C. P. Hess, J. Kurhanewicz, D. B. Vigneron, Hyperpolarized ^{13}C MRI: State of the art and future directions. *Radiology* **291**, 273–284 (2019).
4. V. Ribay, C. Praud, M. P. Letertre, J.-N. Dumez, P. Giraudeau, Hyperpolarized NMR metabolomics. *Curr. Opin. Chem. Biol.* **74**, 102307 (2023).
5. Y. Kim, C. Hilty, Applications of dissolution-DNP for NMR screening. *Methods Enzymol.* **615**, 501–526 (2019).
6. A. Bertarello, P. Berruyer, M. Artelsmair, C. S. Elmore, S. Heydarkhan-Hagvall, M. Schade, E. Chiarparin, S. Schantz, L. Emsley, In-cell quantification of drugs by magic-angle spinning dynamic nuclear polarization NMR. *J. Am. Chem. Soc.* **144**, 6734–6741 (2022).
7. A. Sadet, C. Stavarache, M. Bacalum, M. Radu, G. Bodenhausen, D. Kurzbach, P. R. Vasos, Hyperpolarized water enhances two-dimensional proton NMR correlations: A new approachfor molecular interactions. *J. Am. Chem. Soc.* **141**, 12448–12452 (2019).
8. A. G. Rankin, J. Trébosc, F. Pourpoint, J.-P. Amoureux, O. Lafon, Recent developments in MAS DNP-NMR of materials. *Solid State Nucl. Magn. Reson.* **101**, 116–143 (2019).
9. S. Haber, M. Leskes, Dynamic nuclear polarization in battery materials. *Solid State Nucl. Magn. Reson.* **117**, 101763, 101763 (2022).
10. J. H. Ardenkjær-Larsen, B. Fridlund, A. Gram, G. Hansson, L. Hansson, M. H. Lerche, R. Servin, M. Thaning, K. Golman, Increase in signal-to-noise ratio of > 10,000 times in liquid-state NMR. *Proc. Natl. Acad. Sci. U.S.A.* **100**, 10158–10163 (2003).
11. S. J. Nelson, J. Kurhanewicz, D. B. Vigneron, P. E. Z. Larson, A. L. Harzstark, M. Ferrone, M. van Criekinge, J. W. Chang, R. Bok, I. Park, G. Reed, L. Carvajal, E. J. Small, P. Munster, V. K. Weinberg, J. H. Ardenkjaer-Larsen, A. P. Chen, R. E. Hurd, L.-I. Odegardstuen, F. J. Robb, J. Tropp, J. A. Murray, Metabolic imaging of patients with prostate cancer using hyperpolarized [1-^{13}C] pyruvate. *Sci. Transl. Med.* **5**, 198ra108 (2013).
12. A. Henstra, T.-S. Lin, J. Schmidt, W. T. Wenckebach, High dynamic nuclear polarization atroom temperature. *Chem. Phys. Lett.* **165**, 6–10 (1990).
13. M. Negoro, A. Kagawa, K. Tateishi, Y. Tanaka, T. Yuasa, K. Takahashi, M. Kitagawa, Dissolution dynamic nuclear polarization at room temperature using photoexcited triplet electrons. *Chem. A Eur. J.* **122**, 4294–4297 (2018).
14. T. Hamachi, K. Nishimura, H. Kouno, Y. Kawashima, K. Tateishi, T. Uesaka, N. Kimizuka, N. Yanai, Porphyrins as versatile, aggregation-tolerant, and biocompatible polarizing agents for triplet dynamic nuclear polarization of biomolecules. *J. Phys. Chem. Lett.* **12**, 2645–2650 (2021).
15. T. R. Eichhorn, A. J. Parker, F. Josten, C. Müller, J. Scheuer, J. M. Steiner, M. Gierse, J. Handwerker, M. Keim, S. Lucas, M. U. Qureshi, A. Marshall, A. Salhov, Y. Quan, J. Binder, K. D. Jahnke, P. Neumann, S. Knecht, J. W. Blanchard, M. B. Plenio, F. Jelezko, L. Emsley, C. C. Vassiliou, P. Hautle, I. Schwartz, Hyperpolarized solution-state NMR spectroscopy with optically polarized crystals. *J. Am. Chem. Soc.* **144**, 2511–2519 (2022).
16. N. Matsumoto, K. Nishimura, N. Kimizuka, Y. Nishiyama, K. Tateishi, T. Uesaka, N. Yanai, Proton hyperpolarization relay from nanocrystals to liquid water. *J. Am. Chem. Soc.* **144**, 18023–18029 (2022).
17. F. Alexis, E. Pridgen, L. K. Molnar, O. C. Farokhzad, Factors affecting the clearance and biodistribution of polymeric nanoparticles. *Mol. Pharm.* **5**, 505–515 (2008).
18. G. Kwiatkowski, F. Jähnig, J. Steinhauser, P. Wespi, M. Ernst, S. Kozerke, Direct hyperpolarization of micro- and nanodiamonds for bioimaging applications–Considerations on particle size, functionalization and polarization loss. *J. Magn. Reson.* **286**, 42–51 (2018).
19. D. E. J. Waddington, T. Boele, E. Rej, D. R. McCamey, N. J. C. King, T. Gaebel, D. J. Reilly, Phase-encoded hyperpolarized nanodiamond for magnetic resonance imaging. *Sci. Rep.* **9**, 5950 (2019).
20. G. Kwiatkowski, F. Jähnig, J. Steinhauser, P. Wespi, M. Ernst, S. Kozerke, Nanometer size silicon particles for hyperpolarized MRI. *Sci. Rep.* **7**, 7946 (2017).
21. E. C. Reynhardt, G. L. High, Nuclear magnetic resonance studies of diamond. *Prog. Nucl. Magn. Reson. Spectrosc.* **38**, 37–81 (2001).
22. K.-H. Yang, R. J. Narayan, Biocompatibility and functionalization of diamond for neural applications. *Curr. Opin. Biomed. Eng.* **10**, 60–68 (2019).
23. V. N. Mochalin, O. Shenderova, D. Ho, Y. Gogotsi, The properties and applications of nanodiamonds. *Nat. Nanotechnol.* **7**, 11–23 (2011).
24. J. H. N. Loubser, J. A. van Wyk, Electron spin resonance in the study of diamond. *Rep. Prog. Phys.* **41**, 1201–1248 (1978).
25. E. C. Reynhardt, G. L. High, Dynamic nuclear polarization of diamond. I. Solid state andthermal mixing effects. *J. Chem. Phys.* **109**, 4090–4099 (1998).
26. C. O. Bretschneider, U. Akbey, F. Aussenac, G. L. Olsen, A. Feintuch, H. Oschkinat, L. Frydman, On the potential of dynamic nuclear polarization enhanced diamonds in solid-state and dissolution ^{13}C NMR spectroscopy. *Chem. Phys. Chem.* **17**, 2691–2701 (2016).
27. D. Shimon, K. A. Cantwell, L. Joseph, E. Q. Williams, Z. Peng, S. Takahashi, C. Ramanathan, Large room temperature bulk DNP of ^{13}C via P1 centers in diamond. *J. Phys. Chem. C Nanomater. Interfaces* **126**, 17777–17787 (2022).
28. B. V. Yavkin, G. V. Mamin, M. R. Gafurov, S. B. Orlinskii, Size-dependent concentration of N_0 paramagnetic centres in HPHT nanodiamonds. *Magn. Reson. Solids* **17**, 15101 (2015).
29. Z. Peng, T. Biktagirov, F. H. Cho, U. Gerstmann, S. Takahashi, Investigation of near-surface defects of nanodiamonds by high-frequency EPR and DFT calculation. *J. Chem. Phys.* **150**, 134702 (2019).
30. D. Yoon, M. Soundararajan, S. Sekatski, J. Genoud, S. Alberti, J.-P. Ansermet, High-field 13C dynamic nuclear polarization in nanodiamond. *J. Phys. Chem. C* **123**, 21237–21243 (2019).
31. T. Boele, D. E. J. Waddington, T. Gaebel, E. Rej, A. Hasija, L. J. Brown, D. R. McCamey, D. J. Reilly, Tailored nanodiamonds for hyperpolarized ^{13}C MRI. *Phys. Rev. B* **101**, 155416 (2020).
32. P. London, J. Scheuer, J.-M. Cai, I. Schwarz, A. Retzker, M. B. Plenio, M. Katagiri, T. Teraji, S. Koizumi, J. Isoya, R. Fischer, L. P. McGuinness, B. Naydenov, F. Jelezko, Detectingand polarizing nuclear spins with double resonance on a single electron spin. *Phys. Rev. Lett.* **111**, 067601 (2013).
33. J. P. King, K. Jeong, C. C. Vassiliou, C. S. Shin, R. H. Page, C. E. Avalos, H.-J. Wang, A. Pines, Room-temperature in situ nuclear spin hyperpolarization from optically pumpednitrogen vacancy centres in diamond. *Nat. Commun.* **6**, 8965 (2015).
34. J. Scheuer, I. Schwartz, Q. Chen, D. Schulze-Sünninghausen, P. Carl, P. Höfer, A. Retzker, H. Sumiya, J. Isoya, B. Luy, M. B. Plenio, B. Naydenov, F. Jelezko, Optically induceddynamic nuclear spin polarisation in diamond. *New J. Phys.* **18**, 013040 (2016).
35. A. J. Parker, K. Jeong, C. E. Avalos, B. J. M. Hausmann, C. C. Vassiliou, A. Pines, J. P. King, Optically pumped dynamic nuclear hyperpolarization in ^{13}C-enriched diamond. *Phys. Rev. B* **100**, 041203 (2019).
36. A. Ajoy, K. Liu, R. Nazaryan, X. Lv, P. R. Zangara, B. Safvati, G. Wang, D. Arnold, G. Li, A. Lin, P. Raghavan, E. Druga, S. Dhomkar, D. Pagliero, J. A. Reimer, D. Suter, C. A. Meriles, A. Pines, Orientation-independent room temperature optical ^{13}C hyperpolarization in powdered diamond. *Sci. Adv.* **4**, eaar5492 (2018).
37. K. Miyanishi, T. F. Segawa, K. Takeda, I. Ohki, S. Onoda, T. Ohshima, H. Abe, H. Takashima, S. Takeuchi, A. I. Shames, K. Morita, Y. Wang, F. T.-K. So, D. Terada, R. Igarashi, A. Kagawa, M. Kitagawa, N. Mizuochi, M. Shirakawa, M. Negoro, Room temperature hyperpolarization of polycrystalline samples with optically polarized triplet electrons: Pentacene or nitrogen-vacancy center in diamond? *Magn. Reson.* **2**, 33–48 (2020).
38. M. Gierth, V. Krespach, A. I. Shames, P. Raghavan, E. Druga, N. Nunn, M. Torelli, R. Nirodi, S. Le, R. Zhao, A. Aguilar, X. Lv, M. Shen, C. A. Meriles, J. A. Reimer, A. Zaitsev, A. Pines,

O. Shenderova, A. Ajoy, Enhanced optical ^{13}C hyperpolarizationin diamond treated by high-temperature rapid thermal annealing. *Adv. Quantum. Technol.* **3**, 2000050 (2020).
39. G. Waldherr, J. Beck, M. Steiner, P. Neumann, A. Gali, T. Frauenheim, F. Jelezko, J. Wrachtrup, Dark states of single nitrogen-vacancy centers in diamond unraveled by single shot NMR. *Phys. Rev. Lett.* **106**, 157601 (2011).
40. I. Schwartz, J. Scheuer, B. Tratzmiller, S. Müller, Q. Chen, I. Dhand, Z.-Y. Wang, C. Müller, B. Naydenov, F. Jelezko, M. B. Plenio, Robust optical polarization of nuclear spin baths using Hamiltonian engineering of nitrogen-vacancy center quantum dynamics. *Sci. Adv.* **4**, eaat8978 (2018).
41. Y. Mindarava, R. Blinder, C. Laube, W. Knolle, B. Abel, C. Jentgens, J. Isoya, J. Scheuer, J. Lang, I. Schwartz, B. Naydenov, F. Jelezko, Efficient conversion of nitrogen to nitrogen vacancy centers in diamond particles with high-temperature electron irradiation. *Carbon* **170**, 182–190 (2020).
42. C. Laube, Y. M. Riyad, A. Lotnyk, F. P. Lohmann, C. Kranert, R. Hermann, W. Knolle, T. Oeckinghaus, R. Reuter, A. Denisenko, A. Kahnt, B. Abel, Defined functionality and increased luminescence of nanodiamonds for sensing and diagnostic applications by targeted high temperature reactions and electron beam irradiation. *Mater. Chem. Front.* **12**, 2527–2540 (2017).
43. A. M. Panich, N. A. Sergeev, A. I. Shames, V. Y. Osipov, J.-P. Boudou, S. D. Goren, Size dependence of 13C nuclear spin-lattice relaxation in micro-and nanodiamonds. *J. Phys. Condens. Matter* **27**, 072203 (2015).
44. S. J. Cobb, F. H. Laidlaw, G. West, G. Wood, M. E. Newton, R. Beanland, J. V. Macpherson, Assessment of acid and thermal oxidation treatments for removing sp^2 bonded carbon from the surface of boron doped diamond. *Carbon* **167**, 1–10 (2020).
45. T. Rosskopf, A. Dussaux, K. Ohashi, M. Loretz, R. Schirhagl, H. Watanabe, S. Shikata, K. M. Itoh, C. L. Degen, Investigation of surface magnetic noise by shallow spins in diamond. *Phys. Rev. Lett.* **112**, 147602 (2014).
46. V. M. Acosta, E. Bauch, M. P. Ledbetter, A. Waxman, L.-S. Bouchard, D. Budker, Temperature dependence of the nitrogen-vacancy magnetic resonance in diamond. *Phys. Rev. Lett.* **104**, 070801 (2010).
47. M. Drake, E. Scott, J. A. Reimer, Influence of magnetic field alignment and defect concentration on nitrogen-vacancy polarization in diamond. *New J. Phys.* **18**, 013011 (2016).
48. Y. Mindarava, R. Blinder, Y. Liu, J. Scheuer, J. Lang, V. Agafonov, V. A. Davydov, C. Laube, W. Knolle, B. Abel, B. Naydenov, F. Jelezko, Synthesis and coherent properties of ^{13}C-enriched sub-micron diamond particles with nitrogen vacancy color centers. *Carbon* **165**, 395–403 (2020).
49. G. E. Pake, Nuclear resonance absorption in hydrated crystals: Fine structure of the proton line. *J. Chem. Phys.* **16**, 327–336 (1948).
50. B. Yavkin, M. Gafurov, M. Volodin, G. Mamin, S. B. Orlinskii, in *Experimental Methods in the Physical Sciences* (Elsevier, 2019), pp. 83–113.
51. B. Tratzmiller, J. F. Haase, Z. Wang, M. B. Plenio, Parallel selective nuclear-spin addressing for fast high-fidelity quantum gates. *Phys. Rev. A* **103**, 012607 (2021).
52. Q. Chen, I. Schwarz, F. Jelezko, A. Retzker, M. B. Plenio, Optical hyperpolarization of ^{13}C nuclear spins in nanodiamond ensembles. *Phys. Rev. B* **92**, 184420 (2015).
53. J. Scheuer, I. Schwartz, S. Müller, Q. Chen, I. Dhand, M. B. Plenio, B. Naydenov, F. Jelezko, Robust techniques for polarization and detection of nuclear spin ensembles. *Phys. Rev. B* **96**, 174436 (2017).
54. B. C. Rose, C. D. Weis, A. M. Tyryshkin, T. Schenkel, S. A. Lyon, Spin coherence and ^{14}N ESEEM effects of nitrogen-vacancy centers in diamond with X-band pulsed ESR. *Diam. Relat. Mater.* **72**, 32–40 (2017).
55. S. Felton, A. M. Edmonds, M. E. Newton, P. M. Martineau, D. Fisher, D. J. Twitchen, J. M. Baker, Hyperfine interaction in the ground state of the negatively charged nitrogen vacancy center in diamond. *Phys. Rev. B* **79**, 075203 (2009).
56. A. Shaka, A. Pines, Symmetric phase-alternating composite pulses. *J. Magn. Reson.* **71**, 495–503 (1987).
57. W. Beatrez, A. Pillai, O. Janes, D. Suter, A. Ajoy, Electron induced nanoscale nuclear spin relaxation probed by hyperpolarization injection. *Phys. Rev. Lett.* **131**, 010802 (2023).
58. B. Tratzmiller, "Pulsed control methods with applications to nuclear hyperpolarization and nanoscale NMR," thesis, Universität Ulm (2021).
59. A. Ajoy, B. Safvati, R. Nazaryan, J. T. Oon, B. Han, P. Raghavan, R. Nirodi, A. Aguilar, K. Liu, X. Cai, X. Lv, E. Druga, C. Ramanathan, J. A. Reimer, C. A. Meriles, D. Suter, A. Pines, Hyperpolarized relaxometry based nuclear *T1* noise spectroscopy in diamond. *Nat. Commun.* **10**, 5160 (2019).
60. A. Sarkar, B. Blankenship, E. Druga, A. Pillai, R. Nirodi, S. Singh, A. Oddo, P. Reshetikhin, A. Ajoy, Rapidly enhanced spin-polarization injection in an optically pumped spin ratchet. *Phys. Rev. Appl.* **18**, 034079 (2022).
61. Y. Mindarava, R. Blinder, V. A. Davydov, M. Zaghrioui, V. N. Agafonov, C. Autret, P. Balasubramanian, R. Gonzalez Brouwer, F. Jelezko, "Core–shell" diamond nanoparticles with NV^- centers and a highly isotopically enriched ^{13}C shell as a promising hyperpolarization agent. *J. Phys. Chem. C* **125**, 27647–27653 (2021).
62. G. Winter, N. Eberhardt, J. Löffler, M. Raabe, M. N. A. Alam, L. Hao, A. Abaei, H. Herrmann, C. Kuntner, G. Glatting, C. Solbach, F. Jelezko, T. Weil, A. J. Beer, V. Rasche, Preclinical PET and MR evaluation of ^{89}Zr- and ^{68}Ga-labeled nanodiamonds in miceover different time scales. *Nanomaterials* **12**, 4471 (2022).
63. B. D. Wood, G. A. Stimpson, J. E. March, Y. N. D. Lekhai, C. J. Stephen, B. L. Green, A. C. Frangeskou, L. Ginés, S. Mandal, O. A. Williams, G. W. Morley, Long spin coherence timesof nitrogen vacancy centers in milled nanodiamonds. *Phys. Rev. B* **105**, 205401 (2022).
64. J.-P. Chou, P. Udvarhelyi, N. P. de Leon, A. Gali, Ab Initio study of (100) diamond surface spins. *Phys. Rev. Appl.* **20**, 014040 (2023).
65. J. Kausteklis, P. Cevc, D. Arcon, L. Nasi, D. Pontiroli, M. Mazzani, M. Ricco, Electron paramagnetic resonance study of nanostructured graphite. *Phys. Rev. B* **84**, 125406 (2011).
66. M. L. Goldman, M. W. Doherty, A. Sipahigil, N. Y. Yao, S. D. Bennett, N. B. Manson, A. Kubanek, M. D. Lukin, State-selective intersystem crossing in nitrogen-vacancy centers. *Phys. Rev. B* **91**, 165201 (2015).
67. J.-P. Tetienne, L. Rondin, P. Spinicelli, M. Chipaux, T. Debuisschert, J.-F. Roch, V. Jacques, Magnetic-field-dependent photo dynamics of single NV defects in diamond: An application to qualitative all-optical magnetic imaging. *New J. Phys.* **14**, 103033 (2012).
68. S. Stoll, A. Schweiger, EasySpin, a comprehensive software package for spectral simulationand analysis in EPR. *J. Magn. Reson.* **178**, 42–55 (2006).
69. T. Mittiga, S. Hsieh, C. Zu, B. Kobrin, F. Machado, P. Bhattacharyya, N. Z. Rui, A. Jarmola, S. Choi, D. Budker, N. Y. Yao, Imaging the local charge environment of nitrogen-vacancycenters in diamond. *Phys. Rev. Lett.* **121**, 246402 (2018).
70. A. Webb, Increasing the sensitivity of magnetic resonance spectroscopy and imaging. *Anal. Chem.* **84**, 9–16 (2012).
71. D. J. Lurie, A systematic design procedure for selective pulses in NMR imaging. *Magn. Reson. Imaging* **3**, 235–243 (1985).
72. K. Kobzar, S. Ehni, T. E. Skinner, S. J. Glaser, B. Luy, Exploring the limits of broadband 90° and 180° universal rotation pulses. *J. Magn. Reson.* **225**, 142–160 (2012).
73. A. Ajoy, R. Nazaryan, K. Liu, X. Lv, B. Safvati, G. Wang, E. Druga, J. A. Reimer, D. Suter, C. Ramanathan, C. A. Meriles, A. Pines, Enhanced dynamic nuclear polarization via swept microwave frequency combs. *Proc. Natl. Acad. Sci. U.S.A.* **115**, 10576–10581 (2018).
74. F. E. Mabbs, D. Collison, *Electron Paramagnetic Resonance of d Transition Metal Compounds* (Elsevier, ed. 1, 2013), vol. 16.

Acknowledgments: We acknowledge J. Isoya for providing the single crystal diamond used for pretesting the polarization sequences and J. Bansmann for assistance with XPS acquisition. **Funding:** F.J. and M.B.P. acknowledge support via the ERC Synergy Grant HyperQ (grant no. 856432) and the EU via the project QuMicro (grant no. 01046911). F.J. acknowledges support from the EU via the project FLORIN (grant no. 101086142), QUANTERA via the project "Microfluidics Quantum Diamond Sensor," Carl Zeiss Foundation via IQST, the projects QPHOTON and Ultrasens-Vir, and the DFG. M.B.P. acknowledges support via the EU project SPINUS (grant no. 101135699), the EU project C-QuENS (grant no. 101135359), and the German Federal Ministry of Education and Research (BMBF) under the funding program quantum technologies from basic research to market via the project QuE-MRT (FKZ: 13N16447) and via the project QSens: Quantensensoren für die biomedizinische Diagnostik (QMED) (grant no. 03ZU1110FF). **Author contributions:** R.B. and Y.M. conducted the experiments and analyzed the data. M.K. developed the composite pulses and performed numerical simulations of sequence robustness. R.B. conducted complementary sequence simulations. A.M. performed the automation of the complete hyperpolarization experiment. F.G., S.N. and A.K. contributed to initial simulations of light propagation into diamond powder ensembles and designed the microphotonic structure, for which F.G. optimized the three-dimensional printing process. W.K. and C.L. performed the electron irradiation and annealing and AO. C.J. provided the base material. R.B., Y.M., and M.K. wrote the manuscript with input from all authors. M.B.P., A.K., and F.J. conceived the study. **Competing interests:** The authors declare that they have no competing interests. **Data and materials availability:** All data needed to evaluate the conclusions in the paper are present in the paper and/or the Supplementary Materials.

Submitted 26 May 2024
Accepted 27 January 2025
Published 28 February 2025
10.1126/sciadv.adq6836